The Fibre Multi-Object Spectrograph (FMOS) for Subaru Telescope

Masahiko KIMURA,[1] Toshinori MAIHARA,[2] Fumihide IWAMURO,[2] Masayuki AKIYAMA,[3] Naoyuki TAMURA,[1] Gavin B. DALTON,[5,6] Naruhisa TAKATO,[1] Philip TAIT,[1] Kouji OHTA,[2] Shigeru ETO,[2] * Daisaku MOCHIDA,[2] † Brian ELMS,[1] Kaori KAWATE,[2] Tomio KURAKAMI,[1] Yuuki MORITANI,[2] Junichi NOUMARU,[1] Norio OHSHIMA,[1] Masanao SUMIYOSHI,[2] Kiyoto YABE,[2] Jurek BRZESKI,[4] Tony FARRELL,[4] Gabriella FROST,[4] Peter R. GILLINGHAM,[4] Roger HAYNES,[4] Anna M. MOORE,[4] ‡ Rolf MULLER,[4] Scott SMEDLEY,[4] Greg SMITH,[4] David G. BONFIELD ,[5] § Charles B. BROOKS,[5] Alan R.HOLMES,[5] Emma CURTIS LAKE,[5] Hanshin LEE,[5] ¶ Ian J. LEWIS,[5] Tim R. FROUD,[6] Ian A. TOSH,[6] Guy F. WOODHOUSE,[6] Colin BLACKBURN,[7] Nigel DIPPER,[7] Graham MURRAY,[7] Ray SHARPLES,[7] and, David J. ROBERTSON,[7]

[1]*Subaru Telescope, NAOJ, 650 North Aohoku Place, Hilo, HI, 96720,USA*

[2]*Department of Astronomy, Faculty of Science, Kyoto University, Sakyo-ku,Kyoto,606-8502*

[3]*Astronomical Institute, Tohoku University, Aoba-ku, Sendai, 980-8578*

[4]*Anglo-Australian Observatory, Epping NSW, 1710 Australia*

[5]*Department of Astrophysics, University of Oxford, Keble Road, Oxford OX1 3RH, UK*

[6]*STFC Rutherford Appleton Laboratory, Chilton, Didcot, Oxfordshire, OX11 0QX, UK*

[7]*Department of Physics, University of Durham, South Road, Durham DH1 3LE, UK*

mkimura@subaru.naoj.org

(Received ⟨2010 March 4⟩; accepted ⟨2010 May 27⟩)

Abstract

Fibre Multi-Object Spectrograph (FMOS) is the first near-infrared instrument with a wide field of view capable of acquiring spectra simultaneously from up to 400 objects. It has been developed as a common-use instrument for the F/2 prime-focus of the Subaru Telescope. The field coverage of 30′ diameter is achieved using a new 3-element corrector optimized in the near-infrared (0.9-1.8μm) wavelength range. Due to limited space at the prime-focus, we have had to develop a novel fibre positioner called "Echidna" together with two OH-airglow suppressed spectrographs. FMOS consists of three subsystems: the prime focus unit for IR, the fibre positioning system/connector units, and the two spectrographs. After full systems integration, FMOS was installed on the telescope in late 2007. Many aspects of performance were checked through various test and engineering observations. In this paper, we present the optical and mechanical components of FMOS and show the results of our on-sky engineering observations to date.

Key words: cosmology: observations — instrumentation: spectrographs — telescopes: Subaru — surveys

1. Introduction

In recent years, multi-object spectroscopy surveys on large telescopes have proven to be an essential technique to investigate galaxy formation and other statistical parameters of the Universe. Consequently, most large telescopes now have some kind of multi-object spectrograph. Statistical observations using near-infrared spectrographs have played an important role in the study of galaxy evolution for years. This is largely because the results can be directly compared with studies of local galaxies at optical wavelength. These observations, however, require a considerable amount of telescope time. The multi-object spectrograph in the near-infrared (NIR) wavelength range is the key instrument to make such a study usual.

Using the MOIRCS (multi-object NIR spectrograph) instrument (Suzuki et al. 2009) on the Subaru telescope, it is already possible to obtain spectra from 30-50 objects within a $4' \times 7'$ field of view using cold slit masks. The FMOS instrument however, is capable of acquiring $\sim$ 10 times more objects within $\sim$ 25 times wider field of view. Such a large increase in objects and wide field of view is useful not only for the study of the galaxy evolution and variation with galaxy environment, but also for investigating star-forming regions, cluster formation, cosmology, and so on.

2. Design of the instrument

2.1. Overview

FMOS is a fibre-fed NIR spectrograph of Subaru Telescope (Kimura et al. 2003; Maihara et al. 2000). FMOS has a capability to acquire spectra from 400 targets simultaneously in a 0.9-1.8 μm wavelength range with a field coverage of 30′ diameter at the prime-focus of the telescope (figure 1). FMOS consists of three subsystems; 1) the Prime focus unit for InfraRed (PIR), 2) the fibre positioning system/connector units called Echidna, 3) the two cooled infrared spectrographs (IRS1 and IRS2).

The PIR containing Echidna fibre positioner is mounted on the centre of the top-ring of the telescope. It has an attach-

* Present address: Nikon co., Japan
† Present address: Nagoya City Science Museum, Japan
‡ Present address: Caltech Optical Observatories, California Institute of Technology, 1200 E California Blvd, Pasadena, CA, USA
§ Present address: University of Hertfordshire, UK
¶ Present address: University of Texas at Austin, TX,USA

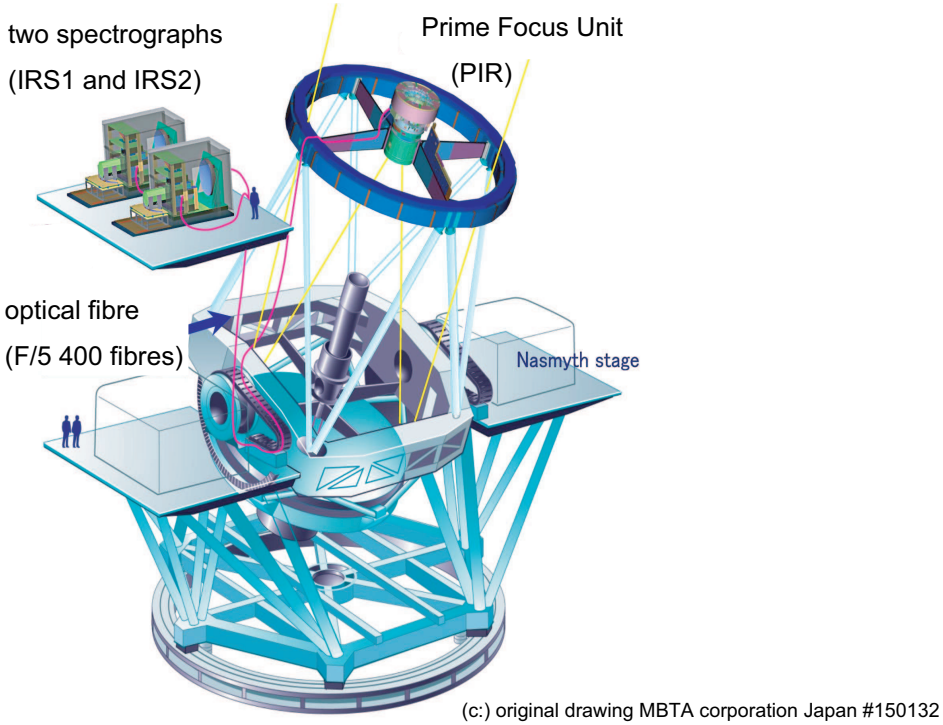

Fig. 1. The mechanical layout of FMOS on Subaru telescope, showing the locations of the prime focus unit (PIR), fi bre bundle, and the two spectrographs (IRS1 and IRS2).

ment mechanism, an optical alignment mechanism, and corrector lens system (figure 2).

Echidna is a novel fibre positioning system collecting light from the 15cm diameter focal plane at the prime-focus of the Subaru Telescope. Tilting fibres are attached to a carbon-fibre "spine" and are moved using a quadrant tube piezo actuator (Brzeski et al. 2004; Gillingham et al. 2000, 2003; Moore et al. 2003). In front of the array of fibres, the Focal Plane Imager (FPI) is located on the XY gantry. The FPI is a dual imaging system capable of measuring the fibre positions for the instrument calibration as well as acquiring sky images for field acquisition. Using several iterations with FPI, Echidna completes a field reconfiguration in less than 15 minutes. The 400 science fibres are divided equally and fed to two cooled spectrographs installed on the fourth floor of the telescope dome (Murray et al. 2003, 2004, 2008). The interconnecting optical feed is a fibre-optic downlink with a length of ~ 70 m.

The two cooled spectrographs have the capability of eliminating strong OH-airglow lines in the J- and H-band, which are the major sources of background radiation at NIR wavelength (Dalton et al. 2006, 2008; Iwamuro et al. 2006, 2008; Lewis et al. 2003, 2004). The suppression system provides a substantial S/N gain for observations at low spectral resolution, thus allowing large simultaneous spectral coverage from a single 2k $\times$ 2k detector (Iwamuro et al. 1994, 2001; Maihara et al. 1993, 1994). To reduce the thermal background in the spectrographs, all of the optics are assembled in a large refrigerator and cooled to below -50°C. Each spectrograph has two modes of spectral resolutions: a high-resolution mode with $\lambda/\Delta\lambda = 2200$ and a low-resolution mode with $\lambda/\Delta\lambda = 500$. The low-resolution mode is realized by using a VPH (Volume Phase Holographic) grating as an anti-disperser. The NIR camera uses a HAWAII-2 HgCdTe detector. It covers the entire J- and H-bands in low-resolution mode.

The conceptual design of FMOS started in 1998, and all the mechanical components were assembled and mounted on the telescope in late 2007. Intensive commissioning observations started in December 2007 and first light was accomplished in May 2008. FMOS is expected to explore various scientific frontiers from nearby substellar objects to the large scale structure of the distant universe.

2.2. PIR: Prime focus unit for IR

2.2.1. Interface mechanism

Subaru Telescope has two prime focus units and three secondary mirrors exchangeable semi-automatically in about six hours in the daytime. One prime focus unit is optimized for a visible light and the other (i.e. PIR) is for NIR wavelength region. The PIR is developed as the front-end unit for FMOS, attached to the centre of the top ring. The Echidna fibre positioner with FPI, and the Shack-Hartmann camera are installed in the instrument bay, which is supported by the outer shell structure with the Focus-Adjustment Mechanism (FAM) and the instrument rotator (figure 2). The corrector lens system is fixed on the bottom of the outer shell structure via the Corrector-Movement Mechanism (CMM) to compensate for the offset of the corrector lens system from the optical axis of the primary mirror with rotation/tilt of the telescope. A computer, cable wrapping system and the fibre connector are also attached to this outer shell structure.

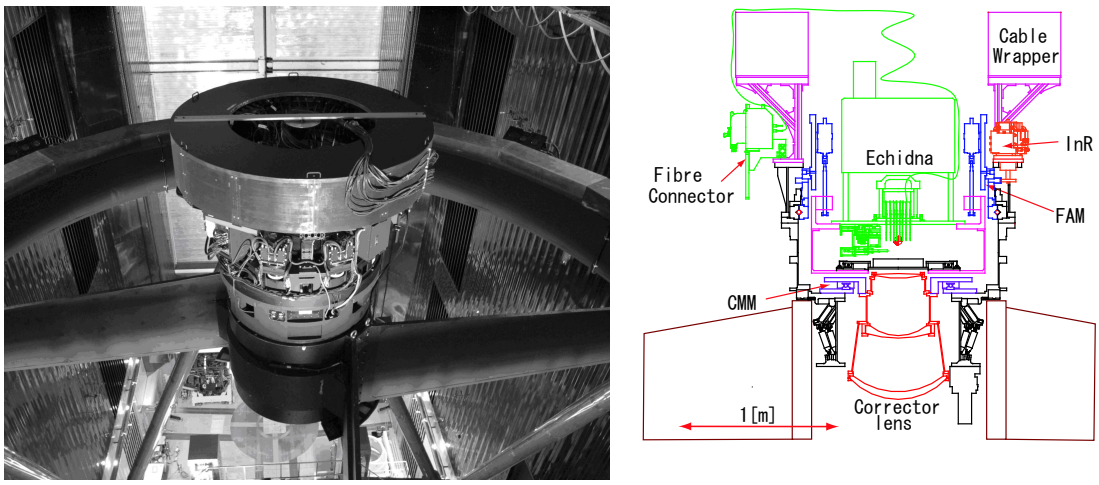

Fig. 2. The prime focus unit attached to Subaru Telescope(left). Sectional drawing of PIR(right).

We can make an optical alignment between the corrector axis and the telescope axis by CMM and FAM using a defocused star image taken by the sky camera of FPI (see 2.3.1). We can also measure the optical aberration of the telescope including the corrector lenses in detail using the Shack-Hartmann camera at the centre of the field. The results of Shack-Hartmann camera are analysed in a series of Zernike's coefficient by the mirror analysis software of Subaru telescope. On the basis of these measurement and corrections, the best XY position of CMM and the best Z position of FAM can be determined as a function of the telescope elevation-angle.

2.2.2. Prime focus corrector

Faint galaxies are considered as main targets of FMOS. The measured intrinsic half-light radius of the faint galaxy is typically $0.''3$ at H=20.5 (Yan et al. 1998). The typical atmospheric seeing is FWHM=$0.''6$ on the summit of Mauna Kea, yields about $0.''9$ diameter for an 80 % energy circle of the faint galaxies. Thus, we select the aperture diameter of the fibre core to $1.''2$ on the sky. This aperture diameter corresponds to about 100 μm on the F/2.1 focal plane of Subaru telescope.

A telecentric focal surface has been chosen to decrease the misalignment between an object and its fibre aperture over the whole field. The three (BSM51Y) spherical lenses of the corrector system allow acquisition over its $30'$ diameter field of view in the NIR wavelength range. The first corrector element has a diameter of 590mm.

The optical aberration of this corrector system is less than $0.''2$ (15μm) in FWHM, small enough compared to the fibre core diameter of $1.''24$ (100μm). The 80% encircled energy diameter is $0.''7$ at the edge of the field of view including the chromatic aberration of magnification (figure 3). In the NIR wavelength range of 0.9-1.8μm, the atmospheric dispersion is $0.''1$ and $0.''3$ at zenith distance of 30 and 60 degrees, respectively. Since these dispersion displacements are considerably smaller than the diameter of the science fibre, we do not use an Atmospheric Dispersion Corrector (ADC).

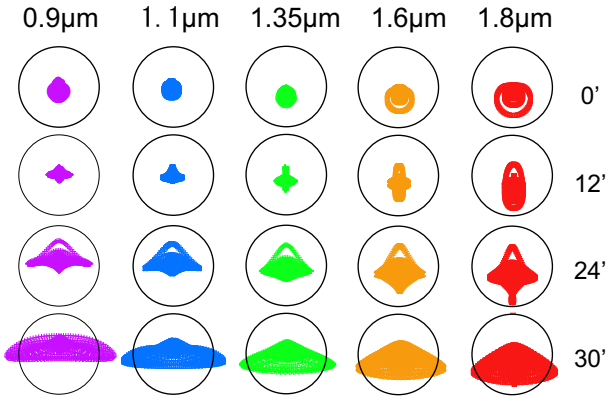

Fig. 3. Spot diagram of the corrector at zenith position. Spots at the wavelengths of 0.9, 1.1, 1.35, 1.6 and 1.8 μm vs. the positions of $0'$(centre), $6'$, $12'$ and $15'$(edge) are plotted. The circle represents the fibre diameter of 100 μm.

2.3. Fibre positioning system

2.3.1. Fibre positioner and focal plane imager

The prime focus of Subaru telescope has a fast F-ratio and a wide field of view, however it is too small (about 150mm in diameter) to use a fibre positioner with magnetic buttons such as 2dF/AAT (Lewis et al. 2002). Therefore we have developed a novel fibre positioning system, Echidna, capable of positioning up to 400 fibres at the prime focus (figure 2). It is based on the use of piezo tube actuators tilting the fibres by electric pulse trains of roughly saw-tooth shape. Each science fibre has a length of $\sim$ 160mm from the tip of the fibre to the pivot ball on the tube piezo actuator, covering a circular area of $\sim$ 7mm in radius by tilting up to 2.5 degrees. The optical loss caused by the tilt to the incident beam is less than 10 % even at maximum tilt. To limit coupling efficiency losses between a target and a fibre, the fibre is positioned within 10 μm of its target.

In order to achieve the required positioning accuracy, we utilise the FPI for spine position feedback (figure 4). The FPI has two cameras; the sky camera and the fibre camera, mounted on the XY stage.

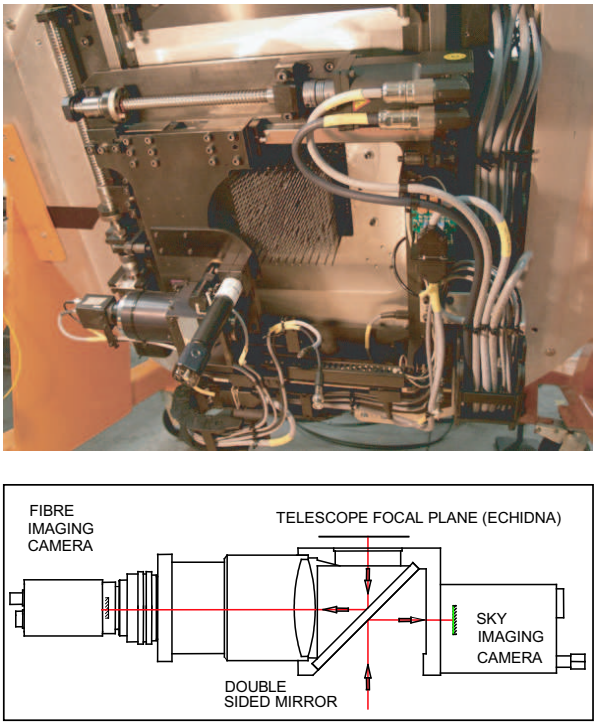

Fig. 4. Echidna fibre positioner with FPI. The fibre camera is used for the fine alignment of the science fibres as well as the guide-fibre bundles, while the sky camera is used for the correction of the initial pointing error of the telescope. The whole view of Echidna, focal plane (top), design of the FPI (bottom).

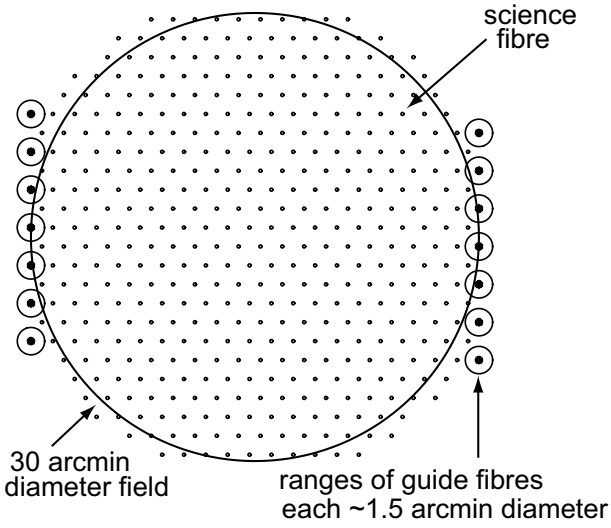

Fig. 5. Layout of 400 science fibres (at home positions) and 14 guide–fibre bundles in focal plane. Circles correspond to the patrol area of the guide-fibre bundles. The guide bundles are attached to spines, positioned by tilting in the same way as science fibres. The fibres in the guide-fibre bundle are closely packed at their input end, while they are separated at the output end to enable an independent intensity measurement by the guiding camera in Echidna.

The sky camera checks the telescope pointing by measuring the positions of several bright stars ($R \leq 15$ AB mag). The fibre camera, which divides the focal plane into 59 small subfields, checks each fibre's position using a back-illumination system. After measuring the positioning error of each fibre from the image taken by the fibre camera, the positioner moves each spine (in parallel) to correct for the error. To achieve a desired positioning accuracy of less than 10μm, this process is repeated ~ 7 times.

Echidna has 14 guide-fibre bundles for auto guiding - they are located on each side of the field. Each guide-fibre bundle consists of 7$\times$50 μm diameter fibres. These bundles are imaged onto a cooled CCD camera through OG570 filter, where stars with R=16.5 mag. or brighter are usable for auto guiding.

2.3.2. Fibre cable and fibre connector

The fibre connector is required to allow the PIR to be removed from the telescope and replaced with other instruments. The connector box is attached to the side surface of the PIR, while the conjugated plug is usually parked at the junction between the centre of the top ring and the spiders. Additionally, the connector has two more roles apart from detaching the PIR unit; 1) conversion of F-ratio from F/2 fibres of Echidna into F/5 fibres of the bundle fed by IRS1 and IRS2, 2) back-illumination of F/2 fibres to flash their tips at the prime focus during the exposure of the fibre camera (Murray et al. 2003, 2004). The incident light at the focal plane has a focal ratio of F/2, which is not optimal when light is to be transmitted through a long fibre. Furthermore, at the spectrograph, such a divergent exit beam would present significant challenges for the design of the spectrograph collimator optics. The expected efficiency of a plano-convex lens coupling in the connector is more than 95% over the wavelength range. The F/2 fibres are 7.6 m long, to cover the routing distance from the focal plane of Echidna to the site of connector. The F/5 fibres are 62 m long, from connector to the spectrographs.

The back-illumination has a movable coupling prism and LEDs which is necessary to measure the exact position of each spine with each exposure on sky.

2.4. Cooled spectrograph

2.4.1. Overview

FMOS has two spectrographs, IRS1 was developed by Kyoto University and IRS2 was developed by University of Oxford and Rutherford Appleton Laboratory, to obtain 2$\times$200 spectra simultaneously in the NIR wavelength range (Dalton et al. 2006, Iwamuro et al. 2006, Kimura et al. 2003, Tosh et al. 2004). Although the mechanical components are completely different, all the optical components and parameters of these spectrographs are identical. Each spectrograph has two spectral resolution modes; the low-resolution mode covers all the wavelength range of 0.9 - 1.8μm with one exposure, while the high-resolution mode requires four exposures at different camera positions to cover the full wavelength range.

The sky background in the NIR region is dominated by many narrow emission lines by OH-airglow. During the night, the OH-airglow lines vary in brightness by 5-10% on a timescale of 5-15 minutes as atmospheric wave flow changes the column density of excited molecules in the line of sight. These strong lines affect not only the background noise at the specified wavelength, but also the stability of the detector itself. These bright OH-airglow lines are suppressed by the mask mir-

ror in the spectrograph. In addition, thermal emission from the optical components is also a considerable noise source. There is no cold stop in the spectrograph: all optical components of spectrograph are cooled in a large refrigerator to keep the temperature below -50 °C (figure 6).

Fig. 6. Two cooled NIR spectrographs. Nearest is IRS2 - the other is IRS1.

2.4.2. *Optics of spectrograph*

The CIRPASS (Cambridge InfraRed Panoramic Survey Spectrograph) instrument, is a fibre-fed and multi-object NIR spectrograph, which has been commissioned by Ian Parry et al (Parry 2004). In the initial design stage, we adopted the optical layout for OH suppression similar to the CIRPASS instrument. Figure 7 shows the optical layout of the spectrograph. These spectrographs are designed to have a capability of OH-airglow suppression by focusing the primary spectra onto the mask mirror using double-path Schmidt optics. The secondary spectra are obtained by the 2048×2048 infrared array detector HAWAII-2 installed in the camera dewar. The length of the incident fibre slit is 12cm, which is reduced to $\sim$ 4cm on the detector.

Although the typical spectral resolution of the primary spectra is $\lambda/\Delta\lambda = 2200$, we can choose the spectral resolution of the secondary spectra $\lambda/\Delta\lambda = 500$ in low-resolution mode ($\lambda/\Delta\lambda = 2200$ in high-resolution mode with (without) the VPH grating, respectively, into the optical path at secondary pupil position to reduce the dispersion given by the first grating. Spectra with the full wavelength range (0.9-1.8μm) are obtained by a single exposure in the low-resolution mode, while four exposures at different camera positions are required to cover the same wavelength range in the high-resolution mode (figure 8).

Each fibre slit contains 200 fibres with a centre-to-centre spacing of 600μm (almost twice the 280μm fibre diameter), which consists of 10 subsets of 20 fibres separated with an additional small spacing between them. The fibres in this fibre slit are arranged in a fan shape along the curvature of the focal sphere of the Schmidt optical system. The output beam is nominally F/5, with up to 10 % of the light emerging into F/4.2 which is controlled back to F/4.7 using field lenses on the output of the slit blocks (Murray et al. 2003).

The spherical camera mirror is a honeycomb light-weight

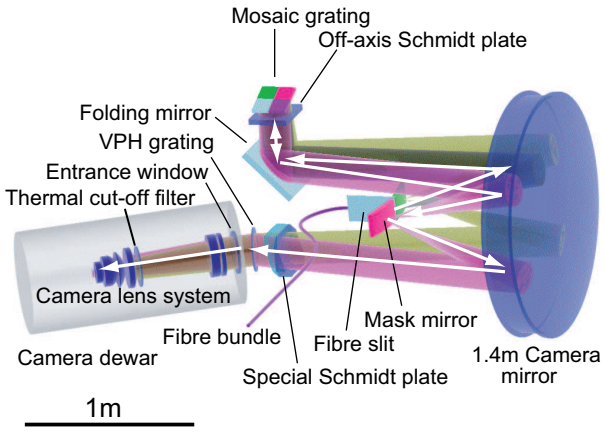

Fig. 7. Optical design of the spectrograph. Optical system from the incident fibre slit to the mask mirror (upper half of the drawing) is the double-path Schmidt system. The reflective mosaic grating and the VPH grating are located at the primary and the secondary pupil, while the primary and the secondary spectra are focused onto the mask mirror and the detector respectively.

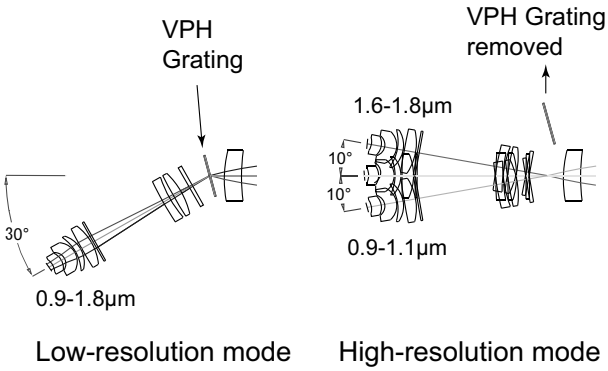

Fig. 8. The position of the camera dewar in each spectral mode.

mirror with a diameter of 1.4m and a weight of 137kg. The radius of curvature is 1940mm. The slit is placed 951 mm in front of the collimator to produce a single beam diameter of $\sim$200mm. The reflective surface is silver with sapphire overcoating.

The off-axis Schmidt plate with dimensions of 280mm × 236mm (× 33mm in thickness) is manufactured using a high-accuracy grinding process (without polishing). The accuracy of the total shape is 0.3μm and the local roughness is 80nm rms. The material is fused silica with anti-reflection coatings on both sides.

The grating at the primary pupil position is composed of 2×2 mosaic of usual reflective gratings with a groove density of 500 g/mm blazed at 1.35μm for the incident angle of 20°, because the diffraction limited performance is not required and the cost reduced considerably. This 2×2 mosaic grating is controlled by using 8 pieces of picomotor actuators for adjustment the direction of the four gratings under refrigerated condition. The total dimensions of this grating is 230mm×210mm.

The mask mirror consists of the two spherical-convex mirrors with a curvature radius of 993mm(figure 9). Each mirror

has dimensions of 280mm$\times$140mm, arranged at both sides of the entrance fibre slit. The gap between these two mirrors corresponds to the atmospheric absorption band at $\sim$1.4μm in the primary spectra focused onto these mirrors. The methods of masking strong OH-airglow lines are different between IRS1 and IRS2. The airglow mask of IRS1 is made of a thin (0.2mm in thickness) stainless-steel plate which is processed by photochemical etching to leave material only at the positions of the strong OH-airglow lines, and blackened to absorb the OH light (Iwamuro et al. 2006). On the other hand, the airglow mask of IRS2 is printed directly on the surface of the mirror by photochemically etching away the reflective gold coating of the mirror so that OH light is absorbed in the substrate and mount of the mirror (Lewis et al. 2004). A total of 283 OH and O_2 airglow lines are rejected on the mask mirror, thus the effective opening area is 78.8 $\%$. The width of the each mask element is 0.4 mm, which is a factor 1.4 times the width of the fibre core diameter of 280 μm on the fibre slit in IRS1. The suppression factor of the OH-airglow line is about 10 and the estimated gain is 1 mag, if observations are sky background limited.

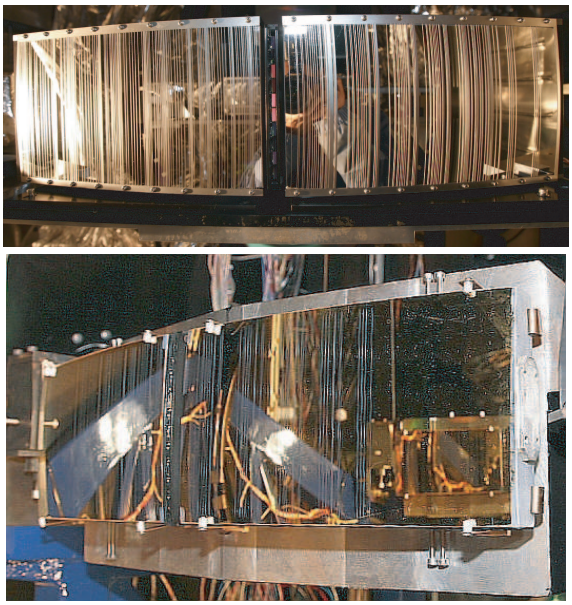

Fig. 9. Mask mirror in IRS1(top) and IRS2(bottom). These masks have patterns of the airglow lines in the J-band and H-band. The airglow mask of IRS1 is made of a thin (0.2mm in thickness) stainless-steel plate at the positions of the strong OH-airglow lines, and blackened to absorb the OH light (Iwamuro et al. 2006). The airglow mask of IRS2 is printed directly on the surface of the mirror by photochemically etching away the reflective gold coating of the mirror so that OH light is absorbed in the substrate and mount of the mirror (Lewis et al. 2004).

The special Schmidt plate has two aspherical concave/convex surfaces with dimensions of 315mm$\times$251mm ($\times$ $\sim$90mm in thickness), which are achieved using a combination of two elements having concave-flat and flat-convex shape (figure 7). Both aspherical surfaces are processed by "ELID" (ELectrolytic In-process Dressing) grinding method. The accuracy of the total shape is 3μm and the local roughness is 100nm rms. The material is fused silica with an anti-reflection coating on both sides of each element.

The VPH grating with a diameter of 262mmϕ and 10mm in thickness is used at the secondary pupil to reduce the dispersion power in the low-resolution mode. The line density is 385 g/mm and the peak of diffraction efficiency is around 1.3 μm at the Bragg condition (Tamura et al. 2003). The material of the substrate is Starphire glass (similar BK7) with anti-reflection coatings on both sides. No significant deterioration has been observed after a number of heating and cooling cycles. Additionally the diffraction efficiency is nearly independent of temperature between 200 and 280 K.

The camera lens system in the dewar consists of 6 spherical lenses (including one aspheric surface), an entrance window, and the thermal cut-off filter with the cut-off wavelength of 1.8μm. The material of all the camera elements is fused silica with the maximum diameter of 250mm. The first order of the axial chromatic aberration of this system is corrected by tilting the detector along the dispersion axis. The focus position and this tilt angle are adjusted to the best position of the selected observation mode.

The designed spot images in the low-resolution mode are shown in figure 10. The 80$\%$ encircled energy diameter is less than 50μm (2.5 pixels) in this mode as well as in the high-resolution mode, smaller than the real image size of a single fibre core of 80μm (4 pixels).

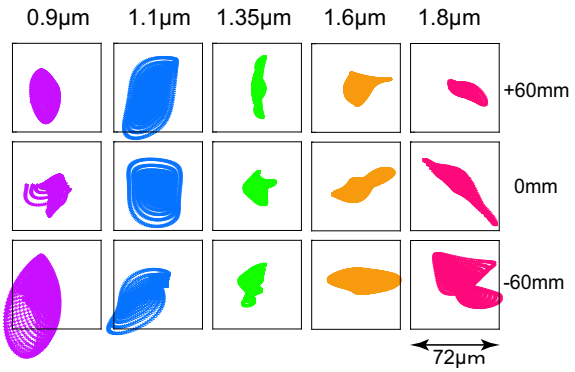

Fig. 10. Spot diagram on the detector in the low-resolution mode. Spots at the wavelengths of 0.9, 1.1, 1.35, 1.6 and 1.8 μm vs. the positions of +60mm(top of the fibre slit), 0mm, -60mm(bottom of the fibre slit) are plotted. The box represents 4 pixels of the detector.

2.5. *Control system*

FMOS control system is designed as a network of subsystem controller PCs. The central PC called FMOS OBCP (OBservation Control Processor) interfaces with the telescope computer system, and also supervises all the FMOS subsystems through the network. The OBCP links to two PIR-dedicated PCs, IRS-dedicated PCs, and Subaru computers. One PIR-PC controls FAM, CMM, and the stage of the Shack-Hartmann system. Another PIR-PC takes part in controlling Echidna positioner as well as the auto guiding signal and FPI system. The IRS-PCs control all the parts of the spectrograph: many cooled optical stages and the dewar stage, the cooling system of refrigerator, and the data acquisition and transfer (Eto et al. 2004, Dipper et al. 2004).

We use two HAWAII-2 array detectors for IRS1 and IRS2

developed by different institutes. The readout electronics of IRS2 camera is a SDSU IR controller system (Leach et al 2000) using the software interface developed for WFCam by the UKATC (Hirst et al. 2006), while that for IRS1 is newly developed one, which adopts the similar front-end circuit of MOIRCS (Ichikawa et al. 2003) combined with the Messia-V system (Nakaya 2004). The Messia-V provides a package of the "Clock Sequencer" and the "Frame Grabber", which has been incorporated in the CCD data acquisition system of the optical instruments of Subaru telescope.

3. Performance

3.1. Engineering observation

The conceptual design started in 1998, and all the mechanical components were assembled and mounted on the telescope in late 2007. Since May 2008, engineering observations have been carried out several times to check the basic performance of FMOS. After measurement of the image quality at the prime focus, the total system efficiency from the corrector lenses to the detector was estimated from the results of these observations as well as from the test using a black body source. The positioning accuracy of Echidna was calibrated using several observations of a part of the galactic plane or open clusters under various conditions. The guiding stability using the guide-fibre bundles was also examined from the dispersion of the error signal during the observations.

3.2. Optical performance of the PIR

In the first stage of our engineering run, we made a rough adjustment of the corrector axis (CMM axis) and the telescope optical axis using a defocused bright-star image taken by the sky camera of FPI. The position of the focus is adjusted by FAM using a star image taken by the same camera. The typical FWHM of the point source is $0\farcs6$ in the optical wavelength.

After the rough positioning, we measured the optical aberration of the telescope including the corrector lenses in detail using the Shack-Hartmann camera at the centre of the field. In this camera, the wave-front error was measured as the position shifts of multiple-images of a single star divided by a micro lens array at the pupil position. The results were expanded in a series of Zernike's coefficient by the mirror analysis software of Subaru telescope. On the basis of these measurement and corrections, the best XY position of CMM could be determined as a function of the telescope elevation angle. The Coma aberration term in the calculated Zernike's coefficients is sensitive to the XY position of CMM, while defocus term corresponds to the position of FAM. We found that the active control of CMM as a function of the elevation angle of the telescope is not necessary at the elevation angle larger than 40°. The aberration coefficient indicates that the spherical and the coma aberration is small enough, while the astigmatism component contributes to the image size of $\sim 0\farcs4$ even at the centre of the field (Kimura et al. 2008).

The tilt and distortion of the focal plane is also checked by the sky camera. We observed the field including an open cluster with tiling the sky camera to determine the direction of the XY axes of FPI coordinate, the pixel scale, and the distortion map of the field. At the edge of the field ($15'$ off-centre position), the position of the star shifts about $10''$ outward because of the distortion. We can identify the optical axis of the telescope including the corrector lenses as the centre position of this distortion pattern. As a results of the distortion measurement, we found the position difference between the rotator axis and the distortion centre is $0'.89$ (4.3mm) - in other words, the distortion pattern moves along a circle during observation. This movement causes $0\farcs24$ shift at the outer edge region of the field for 13° rotation of the instrument rotator. Since neither the optical axis of the telescope nor the rotator axis can be adjustable, we have to readjust ("tweak") a part of the outer fibres blindly between long exposures. No tilt of the focal plane was detected in this measurement.

3.3. Positioning accuracy of Echidna

We measured the displacements of the tips of the fibres whilst changing the elevation angle from zenith to 30 degrees. Almost all the measured displacements are distributed within the range of $50\pm10\mu$m including the displacements of the guide-fibre bundles. Here, the average offset of 50μm has no effect on the positioning accuracy, because the average flexure of the fibres will be cancelled by auto-guiding the telescope using the guide-fibre bundles. The measured scatter is sufficiently small to keep the targets within 10μm ($0\farcs12$) accuracy during a long exposure. Both the stability of the fibre positions in two hours and the measurement accuracy of the fibre camera in FPI are $\sim2\mu$m, negligible compared with the flexure variation of the fibres. Sufficient configuration accuracy can be achieved with 7 iterations of readjustment using FPI (Akiyama et al. 2008): on average 98% of the fibres reach target positions within 10μm at above zenith distance of 60 degree. In each configuration, about 10 fibres cannot reach the target positions due to collisions etc. Since 100 seconds are needed to measure the positions of 400 fibres with the FPI, Echidna takes about 15 minutes to complete 7 iterations.

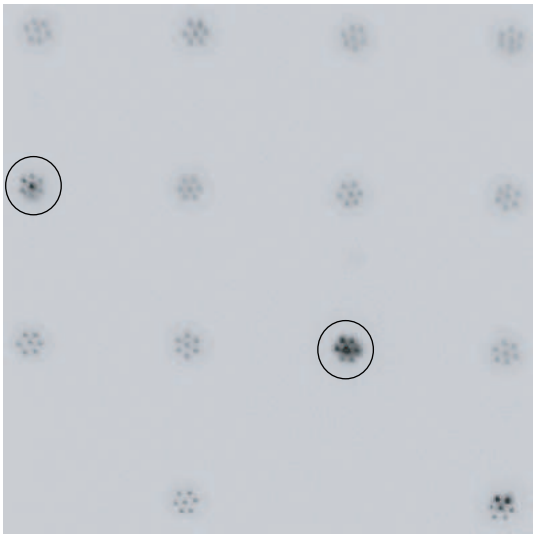

Fig. 11. Image of the guide-fibre bundles. There are 14 bundles each of which consists of $7\times50\mu$m diameter fibres. All fibres are illuminated by sky emission and two bundles indicated with large circles are aligned to guide stars and used for auto-guiding.

The guide-fibre bundle consists of 7 fibres with a core diameter of 50μm arranged in a hexagonal shape with 80μm spacing, which corresponds to 0.″96 at the focal plane. There are 14 guide-fibre bundles located at both edges of the field of view, marked with circles indicating the covering area of $\sim$3′ in figure 5. The images of bright stars acquired by these guide-fibre bundles are shown in figure 11.

The position error for the telescope pointing is calculated by the weighted average of the position offsets of these stars, which is typically less than 0.″18 under the typical sky condition (figure 12). We can expect at least a few guide stars brighter than R=16.5 mag even in the high galactic-latitude area.

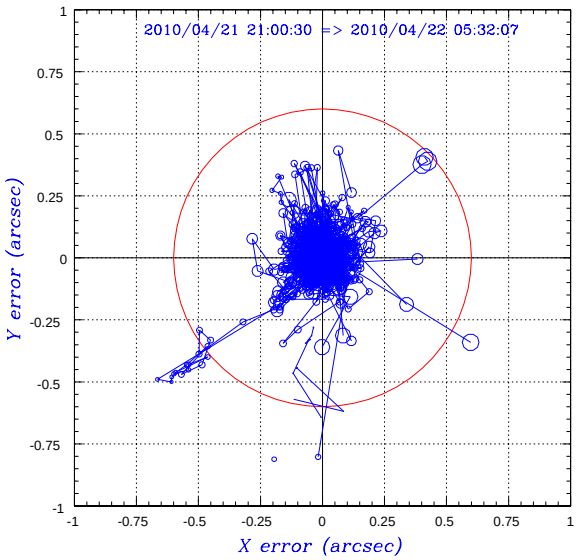

Fig. 12. Distribution of the position error during the auto-guide in the fixed coordinate (XY) to Echidna. The fibre diameter of 1.″2 is indicated by the circle at the centre. Almost all the points located at the outside of the circle are sampled before auto-guiding is started. The size of the symbols corresponds to the averaged brightness of the guide stars. The median auto-guiding error is 0.″067, and typically less than 0.″18.

The position error for each fibre is estimated by ”rastering” of the telescope in a grid pattern around the target position. The map of the observed flux of each object on all the grids of the raster pattern represents the position offset of the target from the science fibre. A maximum of 400 position offsets can be measured simultaneously by this raster sampling method, which determines the configuration accuracy of 0.″15 (figure 13).

3.4. Characteristics of the spectrographs

First, we describe the results of the readout system on the detector. Then, we describe the thermal noise from the optics of spectrograph.

The typical exposure time of FMOS is expected to be $\sim$ 5-15 minutes to observe faint targets. Since very fast readout of the detector compared with the expected exposure time is not required, we operate the HAWAII-2 array with the four-channel readout mode, taking 17 seconds to make a single read with

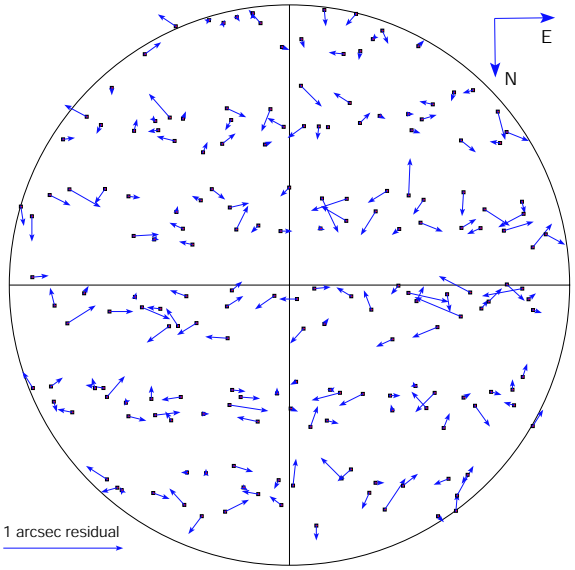

Fig. 13. Position offsets between the targets and science fibres measured by the rastering observation in a open cluster field (NGC6633). The big circle indicates the science field of view of FMOS and each arrow indicates a offset measured with one science fibre. The length of the arrows is exaggerated and the left bottom arrow represents 1.″0 offset. The rms of the offsets is 0.″15. The offsets are random and there is no systematic offsets due to an incorrect distortion pattern modelling.

IRS1, and taking 15 seconds with IRS2. We use ”ramp sampling mode” (iteration of a single read without resetting the detector) in the usual scientific exposure to reduce the contribution of the read-noise of the electronics and also to enable the acquisition of bright objects among faint targets.

The conversion factor and the read-noise of the detector can be estimated from the count-noise diagram derived from many sets of ramp sampling data with a cover attached to the entrance window of the camera dewar. The conversion factor estimated for IRS1 from the diagram is $\sim$ 2.0 electrons/ADU and the readout noise is $\sim$ 22 electrons for a single read (figure 14). The slope of the dashed line is 1/2, which is consistent with shot noise.

Since the maximum ADU count of 2^{16}=65536 corresponding to $\sim 1.3 \times 10^5$ electrons is about half of the full electron capacity of the detector, the non-linearity of the detector is very small even when the count is high. The measured non-linearity is typically less than 1% up to 40000 ADU at IRS1.

When very bright objects are included in the targets, we have to consider two effects on the image; crosstalk and latent images. The crosstalk is identified as ”negative” images on the other quadrant of the detector where the counts are sampled at the same timing as the region with very high counts. The contribution of the crosstalk is about -0.15% of the count of the bright region, correctable in the later data reduction process (figure 15). The latent images are ”positive” patterns remaining after an exposure including highly saturated region, caused by released charges into the conduction band of the detector array. It is difficult to correct the latent images because they depend on various parameters such as incident flux during the previous exposure, elapsed time, temperature, and so on. It takes about 7 minutes until the latent image decays.

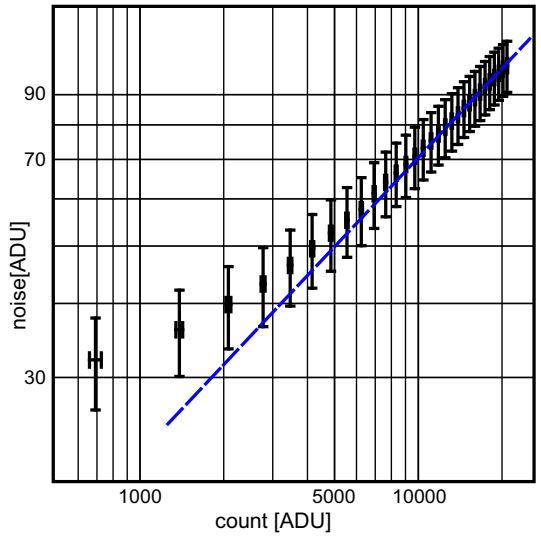

Fig. 14. Conversion factor measurement. The broken line indicates the least square estimation between count and noise. Measured Conversion factor is 2.0 [e$^-$/ADU]. The readout noise is 22 [e$^-$ rms] at IRS1. The dashed line is a least squares fi t to high count data.

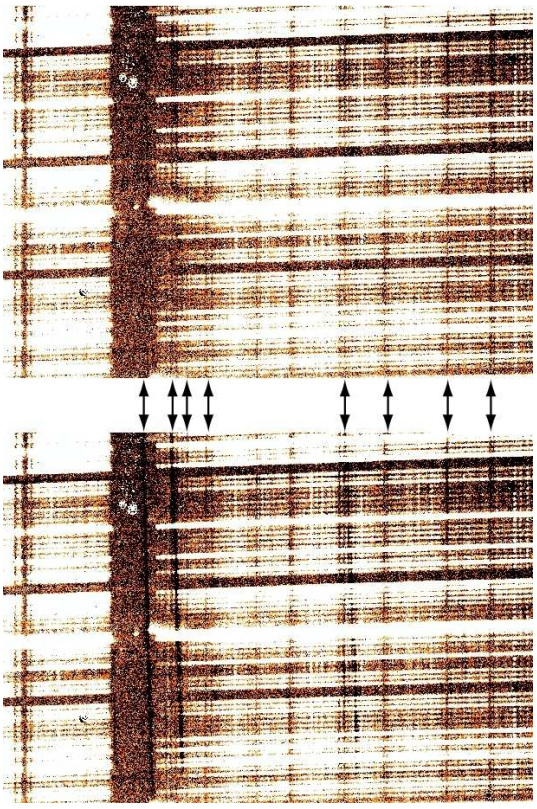

Fig. 15. Correction of crosstalk. The effect of the corrections is presented comparing the image before correction(top) with after(bottom). The positions of the crosstalk images are indicated by the arrows.

The rejection capability of the thermal background of the IRS1 camera part was estimated from the correlation between the background count rate on the detector and the temperature of the refrigerator. In IRS1, we use a normal large refrigerator with pressurised dry air. In IRS2, the cooling is performed with dry chilled air enclosure by a Polycold chiller and ducted into the enclosure. Figure 16 shows the measured background flux for various temperatures of the refrigerator plotted with the expected correlation calculated from the transmission curve of the lens materials and the thermal-blocking filter multiplied by the quantum efficiency of the detector. The measured background flux is consistent with the expected flux indicating that the thermal-blocking filter works effectively.

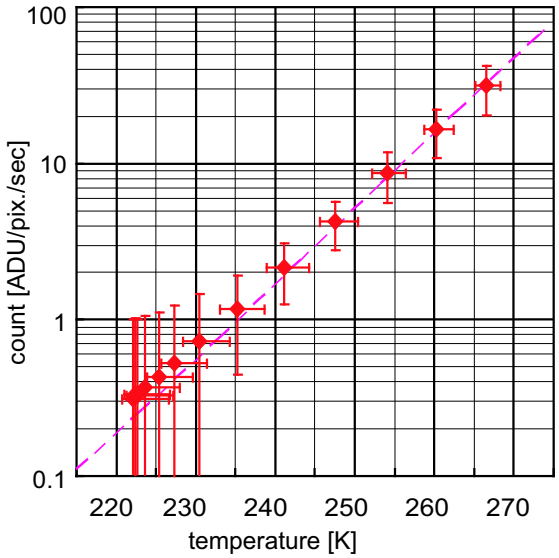

Fig. 16. A background flux as a function of temperature. Points shows the measured background count[ADU/pixel/sec]. The dashed line is an expected thermal background flux.

3.5. Total performance

At first, a black body source with a temperature of 1095$^\circ C$ was attached to the Cassegrain focus to measure the system efficiency. Figure 17 shows the spectra of the blackbody source obtained by IRS1 in the J-long and H-short bands. The typical FWHM of the vertical width of each spectrum is 5 pixels including the optical aberration of 2 pixels, with a pitch of 10 pixels between the spectra (figure 18).

Figure 19 shows the measured efficiencies with low- and high-resolution mode in the full wavelength range. Typical system efficiency for high-resolution mode is 6% in J and 10% in H from the prime focus corrector to the detector, almost consistent with the expected value at high-resolution mode. The decreases of the efficiency in the shorter wavelength side is due to the grating, which has the peak of the diffraction efficiency around 1.35 μm. On the other hand, the decreases in the longer wavelength edge is due to the thermal cut-off filter in the camera dewar. Furthermore, the gradual absorption feature from 1.3μm to 1.4μm is due to the attenuation of the fibre and other silica material used in almost all the lenses. The 1.35 - 1.40 μm

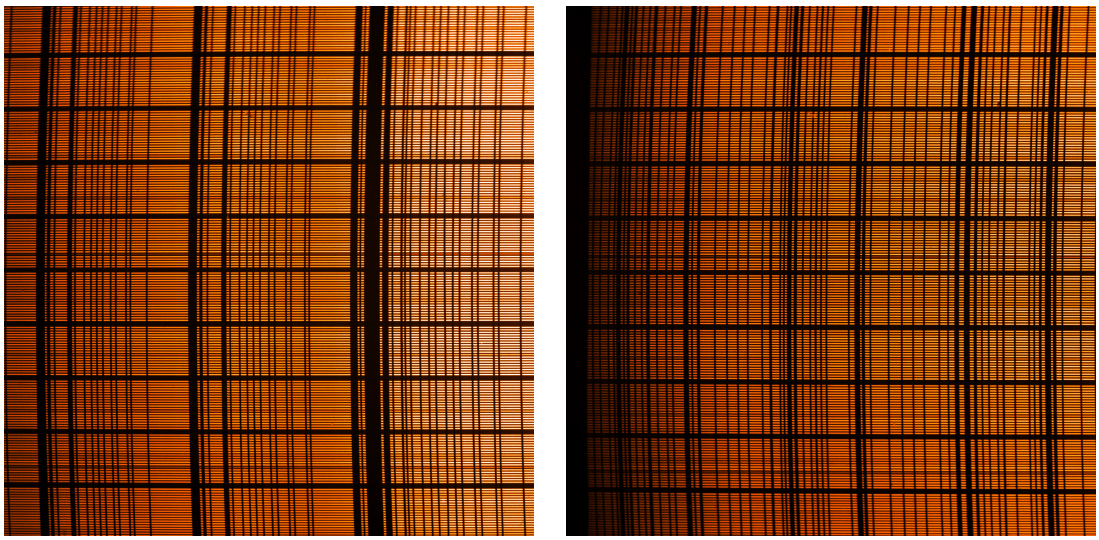

Fig. 17. The spectra of a blackbody emission with a temperature of $1095^{\circ}C$ in the J-long(left) and H-short(right) bands.

part has to be blocked by the fibre slit. Furthermore, these measured efficiencies have about 30 % of the fibre-to-fibre variabilities. These are caused by grime on fibre edges as well as the throughput variety of the fibres including a misalignment of connectors. We also found that the focal ratio degradation effect is not negligible, the factor of $\sim$0.8 estimated from the relative efficiency map for various positions of the black body source on the primary mirror cover.

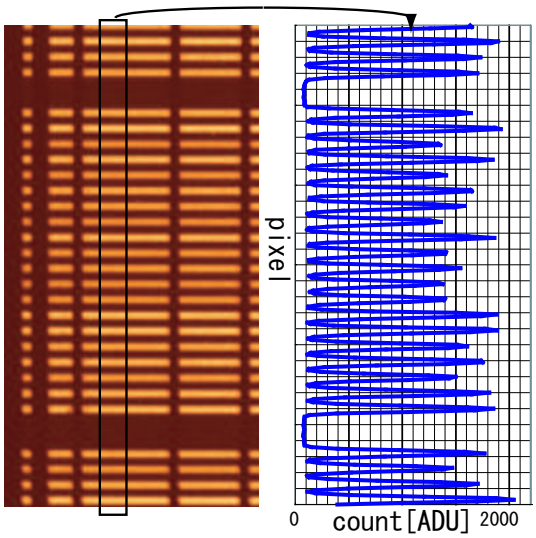

Fig. 18. Closeup view of the figure 17(left). The right panel shows the count(horizontal axis) to pixels (vertical axis, 10 pixel/lines) along the vertical line in the left figure.

We also measured the total efficiency with on-sky observation. There is some difference between the on-sky observation and the blackbody test. One part is the throughput before the corrector; the reflectivity of the primary mirror and the sky transmittance, the other part is the loss at the input surface of fibres; the position error of the fibre, a mis-match of the input

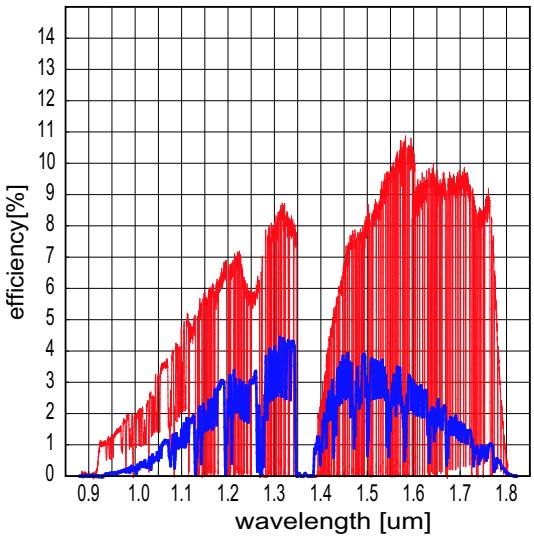

Fig. 19. Absolute efficiencies of the system from the prime focus corrector to the detector include the quantum efficiency of the detector with high- and low-resolution mode. Thin line is the typical(median) value of measured efficiency with high-resolution mode using a blackbody source at 1095 °C, measured by the four exposures of different high-resolution modes. Thick line is the typical(median) value of measured efficiency with low-resolution mode, the throughput of the VPH grating is included. The maximum efficiencies are about 3 % larger than these graphs.

light for the spine-tilt effect, a flux loss for the effect of seeing fluctuation, and the focal ratio degradation effect.

Initially we measured the observational efficiency of the system using an image of a defocused bright star. The measured efficiency is 8% in H bands, almost consistent with the result of the blackbody test assuming the throughput. On the other hand, the total system efficiency based on the observation of an open cluster is 7 ± 3% in H bands, which is factor 0.9 lower than the measured value using the defocused bright star. Therefore, the loss at the input surface of fibres is not

negligible during observations.

The airglow rejection capability of the spectrograph can be tested by scanning the fibre slit along the dispersion direction slightly. Figure 20 shows the variation of the airglow intensity for various offsets of the slit positions, indicating that the mask configuration is not perfect yet. The expected rejection factor of the OH-airglow lines is ~ 10 after we make a little more improvement in the mask to get the maximum performance of the spectrograph.

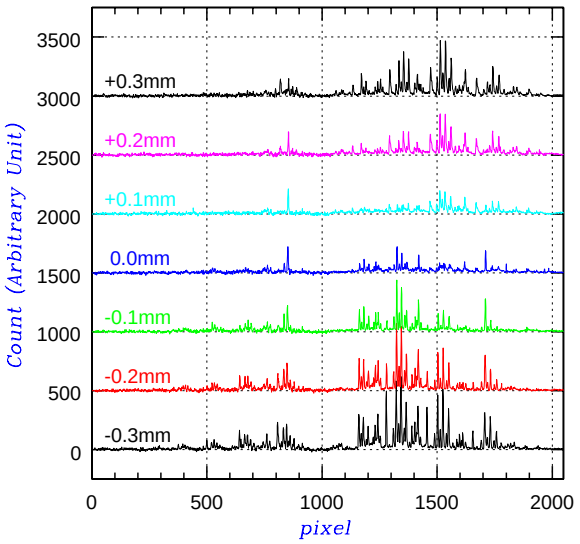

Fig. 20. The variation of the airglow intensity for various offsets of the slit positions from +0.3mm to -0.3mm. The best position is $\sim$ +0.1mm.

Some scientific exposures have been carried out during the engineering observation. Figure 21 shows the reduced spectral image taken in the SXDF (Subaru/XMM-Newton Deep Survey) field from six sets of 15 minutes on- and off-source exposure (total 180 minutes exposure time) in the low-resolution mode. The magnitudes of the four bright stars in this image are around 17 mag. in K-band. The centre gaps in the spectra correspond to the gap between the two mask mirrors where the fibre slit is located.

Although the sky and instrument conditions were not ideal, the estimated limiting magnitudes of continuum flux for an hour exposure with S/N=5 are J =20.1 mag and H =19.8 AB mag in the low-resolution modes. Furthermore, an emission line flux of 1×10^{-16} [erg cm^{-2} s^{-1}] is detected with S/N=5 by 1 hour integration both in J and H.

4. Conclusions

FMOS is a second-generation common-use instrument for the Subaru Telescope, having the capability to simultaneously acquire NIR spectra from up to 400 targets within a 30′ field of view. After all the components were installed on the telescope in late 2007, the total performance was checked through various tests and engineering observations. The major results are as follows.

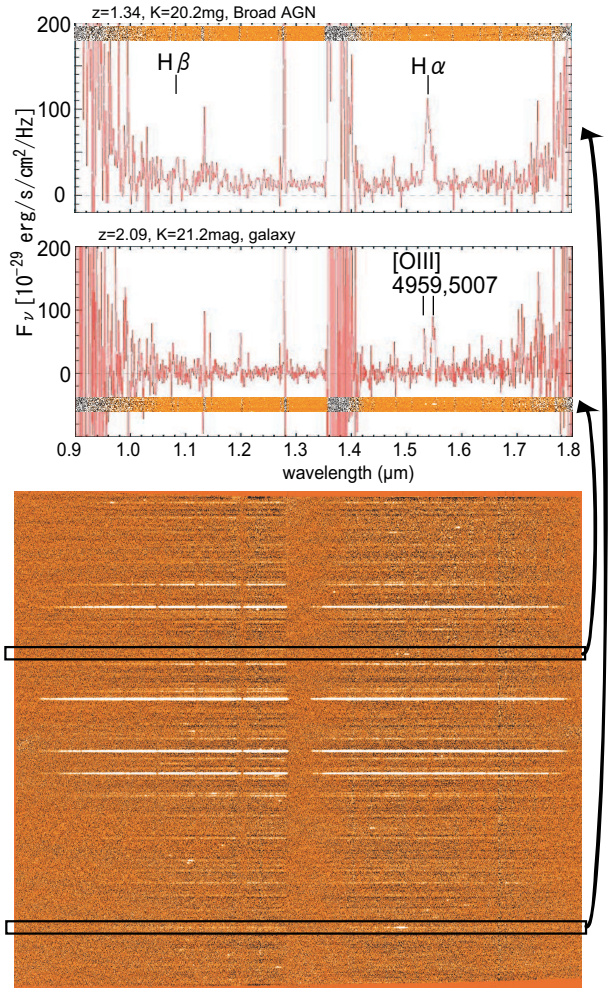

Fig. 21. Two samples of extracted spectra of z=1.34 broad AGN (top) and z=2.09 galaxy (middle) from a reduced spectral image (bottom) in the SXDS field. The wavelength increases from the left (0.9μm) to the right(1.8μm). The bright four spectra are stars for position confirmation. The emission lines is clearly detected Hα and Hβ (upper spectrum), and O[III] (bottom spectrum).

1. Sufficient configuration accuracy can be achieved with 7 iterations using FPI; on average 98% of the fibres reach target positions within 10μm at above zenith distance of 60 degree. Echidna takes about 15 minutes to complete 7 iterations.
2. The configuration accuracy of fibres measured by the raster sampling method is less than 0.″15. The accuracy of auto-guiding using guide-fibre bundles is typically less than 0.″18.
3. The typical system efficiency of 10% from the prime focus corrector to the detector is consistent with the expected value. The total system efficiency of 7% based on real observations is somewhat lower than expected.
4. The rejection capability of the thermal background of IRS1 almost approaches the ideal value, indicating the refrigerator system and the thermal-blocking filter are working well. Although the blocking capability of the OH-airglow mask is currently sub-optimal, a blocking factor of ~ 10 is expected after a little more improve-

ment in the mask.

5. Currently, the limiting magnitudes for a 1 hour exposure with S/N=5 are $J = 20.1$mag and $H = 19.8$ mag in the low-resolution modes. The emission line flux of 1×10^{-16} [erg cm^{-2} s^{-1}] is detected with S/N=5 by 1 hour integration both in J and H. These values were measured from the results of the short observation in the SXDS field.

Although IRS1 has almost been completed, it still has scope for improvement. The blaze-wavelength of the mosaic grating, the cut-off wavelength of the thermal-blocking filter and the deterioration of the total efficiency in low-resolution mode (due to a mis-match of the line density of the VPH grating) can all be improved.

If we use gratings having a shorter blaze-wavelength as well as the thermal-blocking filter with a shorter cut-off wavelength, the limiting magnitude in the J-band will be improved considerably.

Acknowledgment

The FMOS project is managed and operated by the Kyoto university and National Astronomical Observatory of Japan. The present results were accomplished during engineering observation of the Subaru telescope. Tomonori Usuda and Daigo Tomono contributed importantly to the accomplishment of the FMOS project. Kentaro Aoki and operational members support of these engineering observation. We wish to thank Tomio Kanzawa, Yoshitake Nabeshima, Kazuhito Namikawa, Satoshi Negishi, Masami Yutani, and James Ferreira for supporting out test observations at Subaru telescope. The authors wish to thank Day crew members, Telescope group members, and Software members for valuable discussion and continuous support of this work. We also thank Scot Kleinman and Steve Colley for useful comments and suggestions. We would like to express our thanks to the engineering staff of Mitsubishi Co. for their fine operation of the telescope. The UK component of the FMOS project was supported by grants from PPARC (now STFC), and we acknowledge helpful discussions with Ian Parry, Sue Worswick, Derek Ives, Maggie Aderin, and Mattias Wallner. Echidna fibre positioner is managed and developed by the Anglo-Australian Observatory, and we acknowledge helpful discussions with all AAO's staffs. We also thank Hiroshi Karoji and Hiroshi Ohtani for initial contribution of this project. This work was also supported by a Grant-in-Aid for Scientific Research(A), Japan(17204016) and Scientific Research(B), Japan(17403003).

References

Akiyama, M., et al. 2008, Proc. SPIE, 7018, 70182V
Brzeski, K. J., Gillingham, P. R., Correll, D., Dawson, J., Moore, M. A., Muller, R., Smedley, S., and Smith, A. G., 2004, Proc. SPIE, 5492, 1228
Dalton, B. G., et al. 2006, Proc. SPIE, 6269, 136
Dalton, B. G., et al. 2008, Proc. SPIE, 7014, 70143W
Dipper, A. N., and Blackburn, C., 2004, Proc. SPIE, 5496, 565
Eto, S., et al. 2004, Proc. SPIE, 5492, 1314
Gillingham, P. R., et al. 2000, Proc. SPIE, 4008, 1395
Gillingham, P. R., et al. 2003, Proc. SPIE, 4841, 985
Gillingham, P. R., et al. 2006, Proc. SPIE, 6269, 31
Ichikawa, T., Matsumoto, D., Yanagisawa, K., Katsuno, Y., Suzuki, R., Tokoku, C., Asai, K., and Nishimura, T., 2003, Proc SPIE, 4841, 376
Iwamuro, F., Maihara, T., Oya, S., Tsukamoto, H., Hall, N. B. D., Cowie, L. L.,Tokunaga, A. T., and Pickles, A., 1994, PASJ, 46, 515
Iwamuro, F., Motohara,K., Maihara,T., Hata,R., and Harashima,T., 2001 PASJ, 53,355
Iwamuro, F., et al. 2006, Proc. SPIE, 6269, 43
Iwamuro, F., et al. 2008, Proc. SPIE, 7014, 70140T
Kimura, M., et al. 2003, Proc. SPIE, 4841, 974
Kimura, M., et al. 2006, Proc. SPIE, 6269, 132
Kimura, M., Maihara, T., Iwamuro, F., Akiyama, M., Tamura, N., Takato, N., Ohta, K., and Eto, S., 2008, Proc. SPIE, 7014, 70145K
Leach, W. R., and Low, J. F., 2000, Proc SPIE, 4008, 337
Lewis, J. I., et al. 2002, MNRAS, 333, 279
Lewis et al. 2003, Proc. SPIE, 4841, 1108
Lewis, J. I., Dalton, B. G, Band, C., Goodwin, C., and Bonfi eld, G. D., 2004, Proc. SPIE, 5494, 562
Maihara, T., Iwamuro, F., Hall, N. B. D., Cowie, L. L., Tokunaga, T. A., and Pickles,A., 1993, Proc. SPIE, 1946, 581
Maihara, T., Iwamuro, F., Oya, S., Tsukamoto, H., Hall, N. B. D., Cowie, L. L., Tokunaga, Y. A., and Pickles, A., 1994, Proc. SPIE, 2198, 194
Maihara, T., et al. 2000, Proc. SPIE, 4008, 1111
Moore, M. A., Gillingham, P. R., Griesbach, S. J., and Akiyama, M., 2003, Proc. SPIE, 4841, 1429
Murray, J. G., Luke, P., Robertson, J. D., and Tamura, N., 2003, Proc. SPIE, 4943, 184
Murray, J. G., Dodsworth, N. D., Content, R., Tamura, N., Robertson, J. D., Gedge, D., and Brooks, B., 2004, Proc. SPIE, 5492, 1383
Murray, J. G., Dodsworth, N. D., Content, R., Tamura, N., 2008, Proc. SPIE, 7014, 70145K
Nakaya, H., 2004, Proc. SPIE, 5492, 852
Parry, I., 2004, Proc. SPIE, 5492, 1135
Rousselot, P., Lidman, C., Cuby, J. G., Moreels, G., and Monnet, G., 2000, A&A, 354, 1134
Suzuki et al. 2009, PASJ, 60, 1347
Tamura et al. 2003, ExA, 15, 1
Tosh et al. 2004, Proc.SPIE, 5492, 1362
Yan, L., McCarthy, P. J., Storrie-Lombardi, L. J., Weymann, R. J., 1998, ApJ, 503, L19